Influence of Aging Treatment on the Corrosion Susceptibility and Mechanical Properties of Peak-Aged 2195 Al-Cu-Li Alloy

Linyan Xia, Yibo Li, Minghui Huang, Mengxi Chen, and Jinsong Liu

The microstructure, mechanical properties, and intergranular corrosion (IGC) susceptibility of peak-aged 2195 Al-Cu-Li alloy at different temperatures were investigated. The results showed that the microhardness and tensile properties of the alloy were significantly improved by increasing the aging temperature, while the ductility and corrosion resistance decreased. The medium-temperature aged sample could obtain optimal mechanical properties and acceptable corrosion resistance in comparison with other samples. A competitive relationship was observed between T_1 (Al_2CuLi) and θ' (Al_2Cu) phases during aging treatment, where a higher aging temperature promoted nucleation of the T_1 phase, which played the dominant role in strengthening the alloy. However, the θ' phase precipitation was inhibited. The improvement of corrosion susceptibility was mainly related to fine intragranular precipitates, continuous grain boundary precipitates, and a narrow precipitate-free zone. Furthermore, the relationship between the open circuit potential and the IGC sensitivity was discussed to determine the corrosion mechanism of the alloy.

1. Introduction

Due to their low density, high mechanical strength, and good corrosion resistance, Al-Cu-Li alloys have been widely used to fabricate light-weight structures, especially in the aerospace field (Ref [1], [2]). As a typical precipitation-strengthened Al-Cu-Li alloy, AA 2195 alloy has been widely used in aircraft and aerospace structures (Ref [3], [4]).

Recently, many works have demonstrated improvements in the mechanical properties through thermomechanical processing. Li et al. (Ref [5]) showed that both the strength and elongation of an Al-3.7Cu-1.5Li alloy were greatly enhanced by age-forming. Tao et al. (Ref [6]) studied the effect of heat treatment on the mechanical properties of an extruded Al-4Cu-1Li alloy after pre-stretching and artificial aging and found that the yield strength and ultimate tensile strength significantly increased upon increasing the pre-deformation. Chen et al. (Ref [7]) also reported that the mechanical properties of a 2196 alloy were significantly improved by pre-deformation. Furthermore, Al-Cu-Li alloys treated by standard thermal treatment protocols and optimal chemical compositions possess superior mechanical properties (Ref [8]). The contents or the ratio of Cu and Li can affect the tensile strength of Al-Cu-Li alloys, such as 1460, 2050, and 2A96 alloys (Ref [9]). The combined strengthening of the T_1 (Al_2CuLi), δ' (Al_3Li), and θ' (Al_2Cu) phase precipitates was associated with the Cu/Mg ratio (Ref [10]) or the Cu addition (Ref [11]).

Much more attention has been paid to the effects of thermomechanical processing on the corrosion susceptibility of Al-Cu-Li alloys, and research has shown that the corrosion susceptibility changes depending on the different heat treatment temper used (Ref [12], [13]). Guerin et al. (Ref [14]) investigated the corrosion morphologies of 2050 alloy and found that the alloy under T34 and T6 temper showed intergranular and intragranular corrosion, respectively. Such results were demonstrated in another study (Ref [15]), in which the corrosion potential of 2050 alloy decreased after T6 aging treatment due to a change in the corrosion morphology. The intergranular corrosion (IGC) susceptibility of Al-2.58Cu-1.64Li alloy was enhanced by T8 duplex aging compared with T6 aging (Ref [16]). The localized corrosion behavior of Al-Cu-Li alloys at other aging tempers, such as 2099-T83 (Ref [17]), 2A97-T6 (Ref [18]), and 2198-T851 (Ref [19]), has also been extensively investigated.

Actually, the influence of thermomechanical processing on mechanical properties and corrosion susceptibility of Al-Cu-Li alloys depend on the precipitate types and evolution. The general precipitation sequence of Al-Cu-Li alloys is summarized as follows (Ref [20]): GP zones—θ'/θ—δ'—T_1. Different heat treatments can result in different precipitated phases for Al-Cu-Li alloys, where both θ' and T_1 were detected in T6 aging condition, but only T_1 phases were found in T8 aging condition (Ref [21]). Kim et al. (Ref [22]) have reported that the yield strength of 2091 Al-Li alloy was effectively improved by the creation of antiphase of δ' precipitate by dislocation pairs. By contrast, the strength loss of Al-2.81Cu-1.4Li alloy was caused by the decreased number density and coarsening of θ' and T_1 during longer aging treatment (Ref [23]). The work by Li et al. (Ref [5]) on Al-3.7Cu-1.5Li alloy pointed out that the stress

Linyan Xia, Mengxi Chen, and **Jinsong Liu**, Light Alloy Research Institute, School of Mechanical and Electrical Engineering, Central South University, Changsha 410083 Hunan, China; and **Yibo Li** and **Minghui Huang**, Light Alloy Research Institute, School of Mechanical and Electrical Engineering, Central South University, Changsha 410083 Hunan, China; and State Key Laboratory of High-performance Manufacturing, Central South University, Changsha 410083 Hunan, China. Contact e-mail: yibo.li@csu.edu.cn.

during the aging reduced the dimension of T_1 phases, and inhibited grain boundary precipitate coarsening and the PFZ widening, which enhanced the mechanical properties and improved the corrosion resistance.

These previous results indicate that the corrosion resistance and mechanical properties of Al-Cu-Li alloys can be enhanced by controlling their microstructure through a standard heat treatment process. It is well known that the aging temperature during thermomechanical processing greatly influences the precipitate types and distribution. In this case, many investigations have emphasized the influence of aging temperature on the mechanical properties of Al-Cu-Li alloys (Ref 24-26), but few works have investigated the impact of aging temperature on the corrosion susceptibility. It is important to determine how strengthening precipitates are affected by the aging temperature and how this affects their corrosion susceptibility. Therefore, this work systematically studied the impact of different aging temperatures on the corrosion susceptibility, mechanical properties, and microstructure of peak-aged 2195 alloy, especially its IGC susceptibility due to precipitate strengthening. The impact of aging temperature on the electrochemical corrosion of peak-aged 2195 alloy was determined by measuring the potentiodynamic polarization curves and open circuit potential (OCP). These comparative studies provide a relationship between the microstructure and IGC susceptibility of Al-Cu-Li alloys.

2. Materials and Methods

A commercial 2195 Al-Cu-Li alloy developed by Southwest Aluminum Co., Ltd. was used, and its chemical composition is shown in Table 1.

The as-received 20-mm-thick plate was subjected to T0 temper. After hot rolling, the plate was formed into sheets with a thickness of 2 mm. The grains were extended along the rolling (longitudinal, L) direction after hot rolling. The sheets were then subjected to T6 temper by applying solid solution treatment at 530 °C for 1 h, water-quenching, and then different aging treatments were carried out at 140, 160, and 180 °C. The parameters of the T6 temper are shown in Table 2. In the following text, the samples with different aging treatments are referred to as LTA (140 °C), MTA (160 °C), and HTA (180 °C).

Mechanical property tests were performed using three parallel samples to ensure reproducibility. The Vickers hardness values were obtained on a hardness tester (VMH-002UD), with a 500 g loading for 15 s. In addition, the tensile strengths were measured using a CMT-5105GJ machine along the rolling direction with a tensile speed of 2 mm/min.

Specimens for corrosion tests were cut from T6 temper sheets along the rolling direction with a specimen size of 40 mm × 25 mm × 2 mm. Immersion tests of the specimens were performed over 6 h in a solution of 57 g/L NaCl and 10 mL/L H_2O_2 at ambient temperature. Then, the tested surface along the longitudinal-longitudinal transverse (L-LT) plane was exposed to the electrolyte, as shown in Fig. 1. Under these conditions, the corroded specimens were cut along their cross-section for corrosion morphology observations. Corrosion defects were observed by scanning electron microscopy (SEM) on a Hitachi

Table 1 Chemical compositions of the studied alloy (wt.%)

Li	Cu	Mg	Ag	Mn	Zr	Al
1.1	4.09	0.34	0.35	0.34	0.08	Balance

SU1510 equipped with an energy-dispersive spectrometer (EDS) facility. EDS measurements were performed with an accelerating voltage of 25 KV, a takeoff angle of 35° and the elapsed live time of 30. Finally, a FEI Titan G2 60-300 TEM equipped with a high-angle annular dark-field (HAADF) detector was used to clarify the role of precipitation on the corrosion susceptibility of 2195 alloy.

The open circuit potential (OCP) and the polarization of the studied alloy were measured in a 3.5% NaCl solution by a Corr Test CS300 electrochemical workstation. OCP measurements were performed using an Ag/AgCl reference electrode for 0.5 h to obtain a relatively stable value. The polarization curves were scanned from -0.3 $V_{Ag/AgCl}$ to 0.3 $V_{Ag/AgCl}$ with respect to the OCP at a scan speed of 1 mV/s. The polarized specimens were immersed in a mixed solution containing 20 g Cr_2O_3, 50 ml H_3PO_4, and 950 ml deionized water for 10 min to remove the corrosion products. The three-dimensional corrosion morphology was observed by a laser scanning confocal microscope (Zeiss Axio LSM 700) after removing the corrosion products.

3. Results

3.1 Microhardness and Tensile Properties

Figure 2 illustrates the age-hardening curves of 2195 alloy under different aging temperatures. When the LTA sample was aged for 168 h, the peak hardness reached 155.63 HV. At aging temperatures of 160 °C and 180 °C, the peak hardness was reached in 96 h and 24 h, respectively; thus, the peak-aged condition decreased, while the age-hardening rate increased upon increasing the aging temperature. Figure 2 also shows that a higher aging temperature increased the peak hardness, comparing the LTA and MTA samples; however, there is only a slight increase when the metallurgical state changed from MTA to HTA.

Figure 3 shows the representative stress-strain curves of peak-aged 2195 alloy for each condition. It can be seen that both the yield strength and tensile strength gradually increased upon increasing the aging temperature. The parameters of tensile properties of the studied alloy at different aging temperatures are shown in Fig. 4. Compared with the LTA sample, the MTA sample showed much higher tensile strength (530 MPa) and yield strength (495 MPa). Similar to the peak hardness, there was very little change in the strength between the MTA and HTA samples. Namely, the peak tensile and yield strengths were achieved using the MTA conditions. In addition, the elongation of the samples decreased upon increasing the aging temperature. Compared with the LTA sample, the elongation of the MTA and HTA samples decreased by 40.3% and 45.5%, respectively.

**Table 2 Parameters of different T6 treatments of 2195 Al-Li alloy**

| Description of the tests	Low-temperature aged (LTA)	Medium-temperature aged (MTA)	High-temperature aged (HTA)
Artificial aging temp	140 °C	160 °C	180 °C
Peak-aging temp./time	140 °C/168 h	160 °C/96 h	180 °C/24 h
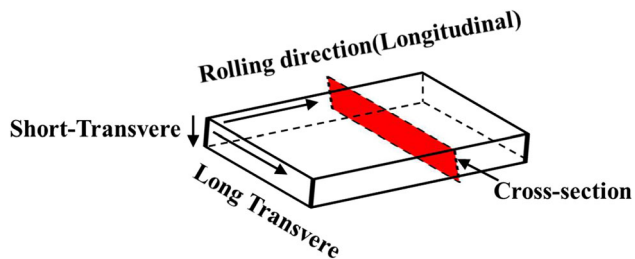
Fig. 1 Schematic diagram of the corrosion sample
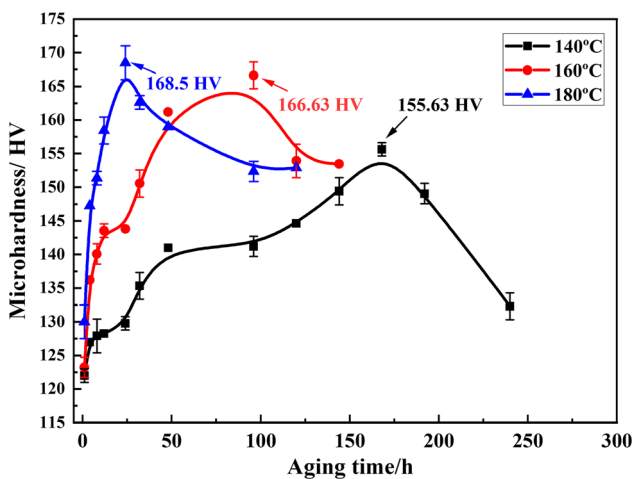
Fig. 2 Age-hardening curves of the samples at different aging temperatures
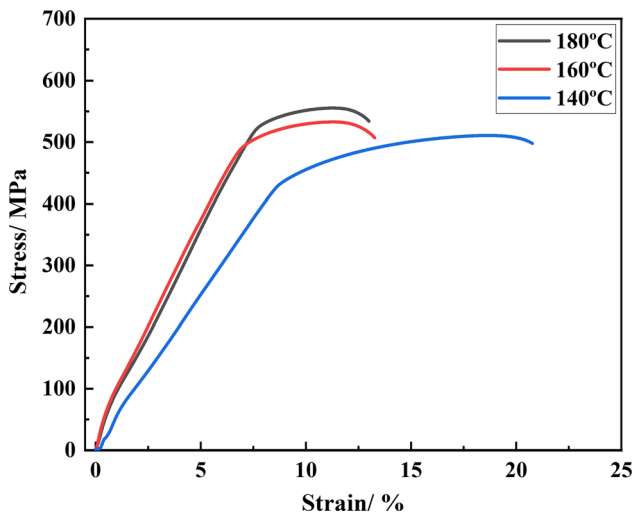
Fig. 3 Stress-strain curves of peak-aged 2195 alloy at different aging temperatures
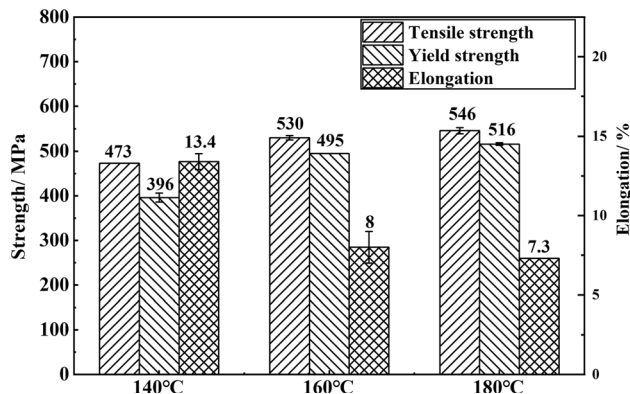
Fig. 4 Tensile properties of peak-aged 2195 alloy at different aging temperatures

3.2 Corrosion Susceptibility

3.2.1 Intergranular Corrosion. SEM observations of representative corrosion morphologies of 2195 alloy are shown along the ST direction in Fig. 5. Typical local IGC damages, pitting corrosion, and intragranular corrosion were observed. Moreover, the statistical analysis data of the IGC depth are given in Table 3. The average and maximum propagation depths continued to increase upon increasing the aging temperature, showing that the aging temperature has a significant effect on the IGC susceptibility. These results confirmed that the HTA sample exhibited the lowest intergranular corrosion resistance of all samples.

To better understand the characteristics of the corrosion damage under the HTA conditions, the enlarged views of different corrosion areas of the HTA sample are shown in Fig. 6. Both intergranular and intragranular corrosion defects can be clearly observed, but no such defects were found in the LTA and MTA samples. The IGC resistance of the alloy decreased upon increasing the aging temperature. Furthermore, Fig. 6(d) shows the EDS analysis and corrosion micrographs of the HTA samples after immersion in 0.97 M NaCl solution. The narrow and dark lines at the corroded grain boundaries indicate the dissolution of grain boundaries, which clearly show that the HTA sample is susceptible to both intergranular and intragranular corrosion. Comparing the element contents in the grain interior (point 1) and at the grain boundary (point 2) shows that the oxygen content was much higher at the grain boundary, but the Cu element content only slightly changed. The grain boundary was highly reactive to the environment in terms of the increased level of oxygen (Ref 17), indicating that the intergranular corrosion of HTA samples was much worse than intragranular corrosion. Moreover, other coarse particles can also be found in the HTA samples, such as the white particles of the Al-Cu-Fe phase (point 3) at un-corroded sites. Point 4 in the matrix consists of Al and Cu atoms, indicating that the Cu
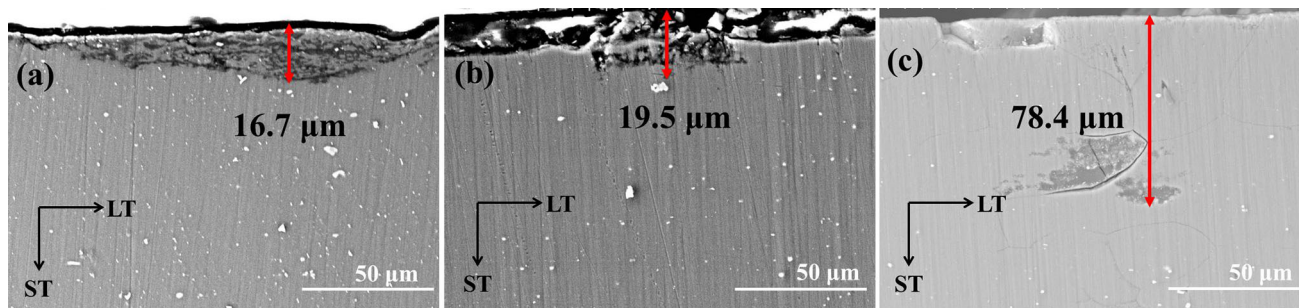
Fig. 5 SEM images of the corrosion depths in the cross-sections of (a) LTA, (b) MTA, (c) HTA samples

Table 3 Intergranular corrosion depths of peak-aged 2195 alloy

Aging condition	Average depth/μm	Maximum depth/μm
LTA, 140 °C/168 h	12.9	16.7
MTA, 160 °C/96 h	15.1	19.5
HTA, 180 °C/24 h	72.6	78.4

Table 4 OCP and electrochemical parameters of 2195 alloy

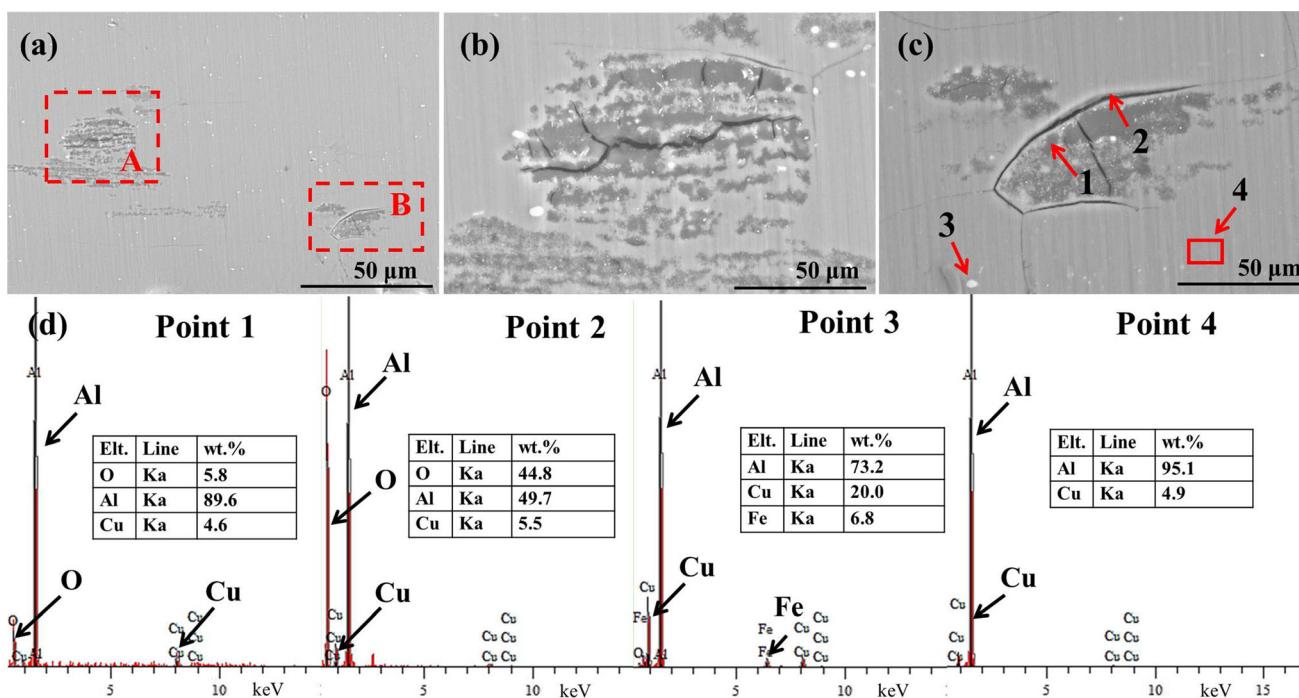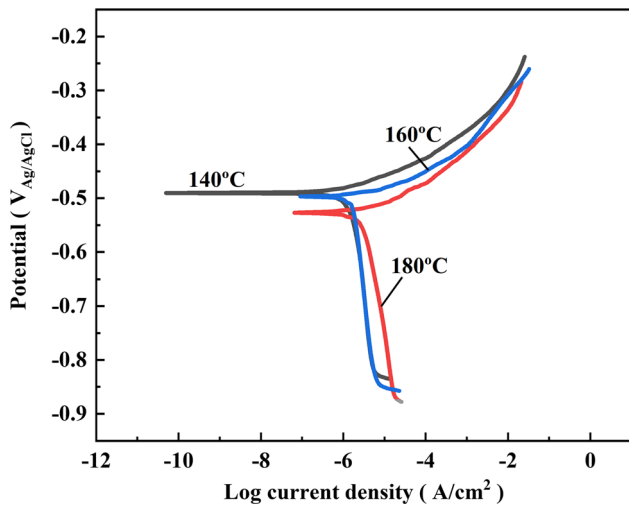| Aging condition	OCP, $V_{Ag/AgCl}$	E_{corr}, $V_{Ag/AgCl}$	I_{corr}, A/cm^2
LTA, 140 °C/168 h	−0.531	−0.49	2.46×10^{-7}
MTA, 160 °C/96 h	−0.637	−0.50	8.22×10^{-7}
HTA, 180 °C/24 h	−0.653	−0.53	9.69×10^{-7}

Fig. 6 (a) SEM images of IGC defects for HTA samples; (b), (c) the framed area in (a) at increased magnification; (d) EDS analysis of particles in (c)

content of the matrix was slightly different from the grain boundary. As demonstrated in previous studies (Ref 10, 27, 28), chemical heterogeneity along a grain boundary can produce intergranular corrosion, which is related to the grain boundary precipitates and precipitate-free zone (PFZ). The relationship between the grain boundary precipitates, PFZ, and the corrosion susceptibility will be discussed later.

3.2.2 Electrochemical corrosion and OCP. To more clearly analyse the corrosion susceptibility of LTA, MTA, and HTA samples, the open circuit potentials and potentiodynamic polarization curves were obtained in 3.5% NaCl solution. Table 4 shows the OCP measurements as a function of aging temperature, and the OCP values decreased slightly from −0.531 V to −0.653 V upon increasing the aging temperature.

The three curves in Fig. 7 display the same shape, with an active anodic region and a plateau cathodic region. The

corresponding corrosion parameters that were extracted from the curves using Tafel extrapolation suggest that the LTA sample exhibited a higher corrosion potential (E_{corr}) and a lower corrosion current density (I_{corr}) than other samples (Table 4). In generally, the corrosion rate can be directly revealed by the corrosion current density, and higher I_{corr} values are related to a higher corrosion sensitivity (Ref 29). In other words, the LTA sample was less susceptible to corrosion; therefore, it displayed the lowest IGC depth than the others, which is in accordance with the IGC test results. Furthermore, the corrosion parameters of the three samples were related to the microstructure after different aging treatments.

As shown in Fig. 8, localized corrosion damage was observed in the SEM micrographs of LTA, MTA, and HTA samples after potentiodynamic polarization in 3.5% NaCl solution. The corrosion first extended inside an entire grain (Fig. 8d) and then propagated in the rolling direction. It can be seen that increasing the aging temperature produced widespread corrosion defects. Compared with other specimens, much more localized corrosion areas were observed on the HTA sample.

Figure 8 also shows high-magnification images of the corrosion morphology on LTA and MTA samples after potentiodynamic polarization tests (Fig. 8d-k). For the LTA sample, corrosion propagated along grain boundaries and also in the grain (Fig. 8d and e). The slightly corroded grain interior after the boundary attack indicates that the sample was only slightly attacked by the corrosive media (Fig. 8f). In contrast, severe corrosion was observed throughout the grain interior of the MTA sample (Fig. 8g). In addition to an increased number of corrosion defects, some cavities and trenches around intermetallic particles (indicated by the arrows) were also observed within the grains (Fig. 8h and k).

Fig. 7 The polarization curves of the studied alloy at different temperatures
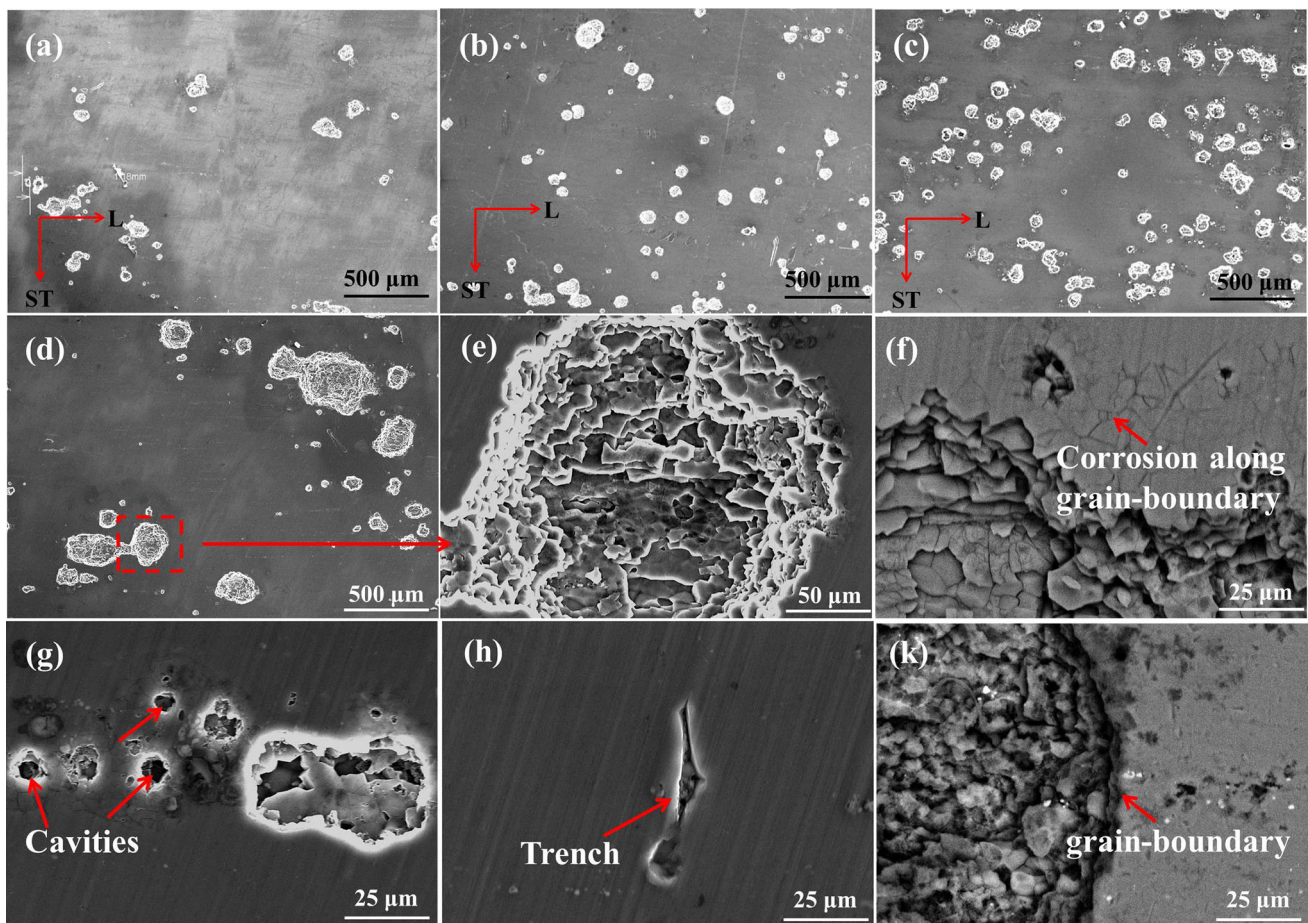
Fig. 8 SEM micrographs of the (a), (d)-(f) LTA, (b), (g)-(k) MTA, and (c) HTA samples after potentiodynamic polarization
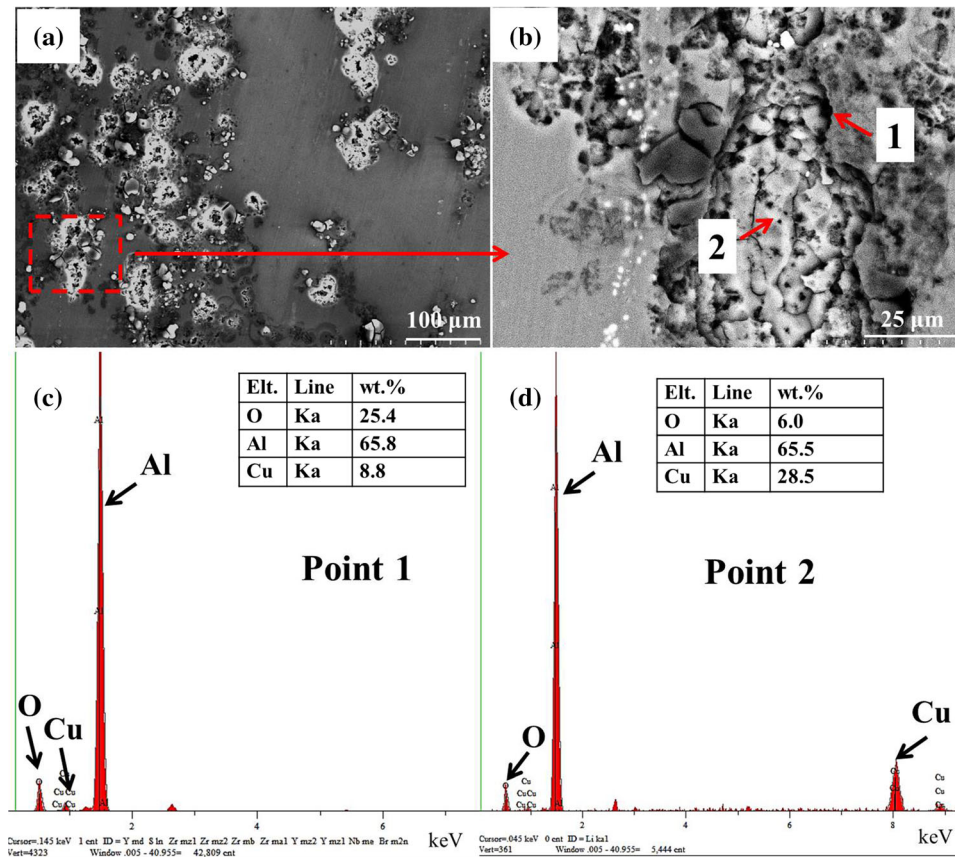
Fig. 9 SEM micrographs of (a), (b) HTA samples after potentiodynamic polarization; (c),(d) EDS results of particles in (b)

Based on previous analysis, the corrosion resistance of the HTA sample was lower than other specimens, which was revealed by the highly different corrosion morphologies shown in Fig. 9(a) and (b). To further investigate the corrosion damage, EDS patterns obtained from points 1, and 2 in Fig. 9(b) are given in Fig. 9(c) and (d), respectively. Strong chemical heterogeneities were observed along the corroded grain boundaries and within the grain interior. The EDS spectrum indicates that a higher oxygen content and a lower copper content were detected along the grain boundaries, compared with the grain interior.

The three-dimensional (3D) images of the corroded samples are compared in Fig. 10. The images show (Fig. 10a, c, and e) that the HTA sample exhibited much more serious localized corrosion than other samples. The 3D surface morphologies with non-uniform hemispherical isolated cavities confirm that the three samples exhibited a similar type of localized corrosion. In addition to an increased number of areas with severe localized corrosion, many homogenized cavities were observed on the HTA sample. For the MTA sample, there are some large aggregated cavities, while a few dispersed cavities were distributed in the LTA sample; however, these cavities presented a similar shape, which indicates that the three samples were corroded by the same corrosion initiation. Moreover, the average depth of the cavities increased slightly (varying from 71, 78, to 83 μm) upon increasing the aging temperature. Increasing the aging temperature accelerated localized corrosion on the surface of the samples after potentiodynamic polarization tests. Such results are in agreement with the above SEM analysis (Fig. 8).

3.3 Microstructural Characterization

In Fig. 11, the STEM images and corresponding selected area electron diffraction (SAED) patterns along the $[011]_{Al}$ direction of different samples demonstrate some details of precipitate evolution. The diffraction spots of the T_1 (Al_2CuLi) phase appear at 1/3 and 2/3 $\{02\overline{2}\}_{Al}$ through $\{110\}_{Al}$, and those at $1/2\{200\}_{Al}$ indicate the presence of the θ' (Al_2Cu) phase along $\{100\}_{Al}$ (Ref 30). In the diffraction patterns in Fig. 12, the T_1 and θ' phases are clearly observed. Upon increasing the aging temperature, T_1 precipitates became finer and more densely distributed. In contrast, θ' precipitates became coarser and more sparsely distributed.

To better describe changes in the size and number density of θ' and T_1 phases with the aging temperature, statistical analysis was performed using Nano-Measure 1.2 software. The microstructural parameters calculated from more than 300 precipitates for each aging condition are summarized in Fig. 12 and Table 5. Upon increasing the aging temperature, the number density and area fraction of T_1 precipitates increased, while the average length and width slightly decreased. For θ' precipitates, the opposite trend was obtained. The number density of θ' phases in the LTA sample is 503.35 μm^{-2}, while that in MTA and HTA samples remarkably decreased to 79.43 and 39.23 μm^{-2}, respectively. Moreover, the average width of θ' and T_1 phases remained a little change.

It is notable that in all three samples, very few T_1 precipitates with lengths exceeding 250 nm were observed, and the average value varied in a small range of 128.44 nm in the HTA sample to 133.59 nm in the LTA sample. In contrast,
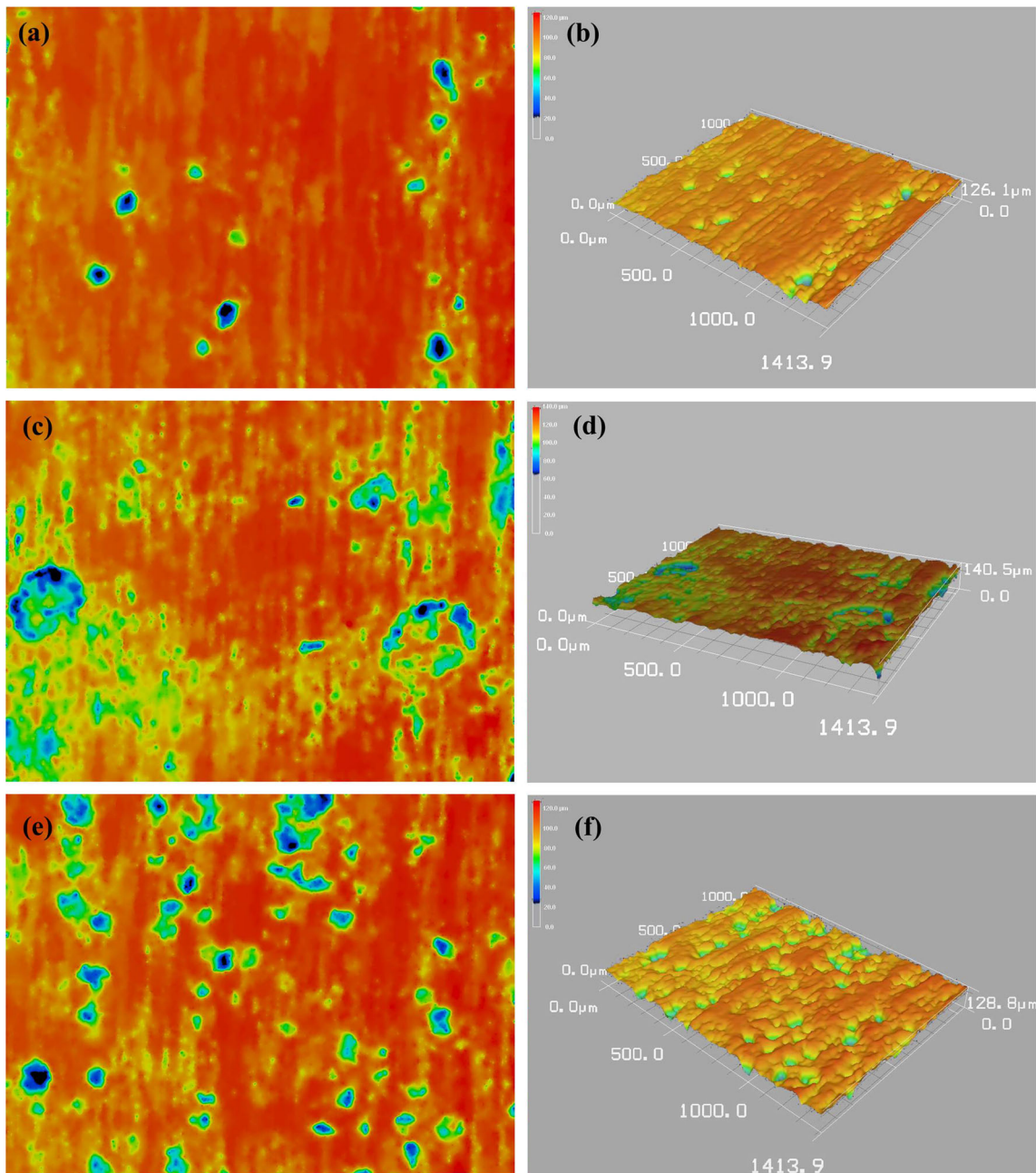
Fig. 10 Typical surface micrographs of the (a) LTA, (c) MTA, (e) HTA samples after potentiodynamic polarization; (b), (d), (f) three-dimensional images

the average length of θ' precipitates increased tremendously from 29.23 nm in the LTA sample to 77.74 nm in the HTA sample. That is, precipitation is competitive between θ' and T_1 phases. Jiang (Ref 31) proposed that the θ' and T_1 phases competed with each other for Cu solute atoms, so their distribution and number density in the matrix were affected by the different aging processes. Li (Ref 5) also found the competitive precipitation relationship between θ' and T_1 phases, where the T_1 phase consumed many Cu atoms, which inhibited the θ' phase precipitation due to the lack of a precipitation driving force. In this work, the high aging temperature significantly facilitated the aging process, leading to an increase in the number density and area fraction of T_1 phases. However, the average width and length of T_1 phases

were insensitive to the aging temperature, and the lack of Cu atoms made it difficult to continue growing the T_1 phase, resulting in their little decrease. Such results may be responsible for the different corrosion susceptibility and mechanical properties of the studied alloy.

Figure 13 shows the presence of some intergranular T_1 phases and a few intergranular θ' phases at the grain boundaries of all samples. For the LTA sample, the PFZ with a width of 103 nm accompanied by discontinuous grain boundary precipitates can be clearly distinguished (Fig. 13a and b). As the aging temperature increased, the PFZ became thinner, and more intergranular T_1 phase appeared along the grain boundary. Especially in the HTA sample, the PFZ was not observed, and the grain boundary precipitates became continuous. The grain
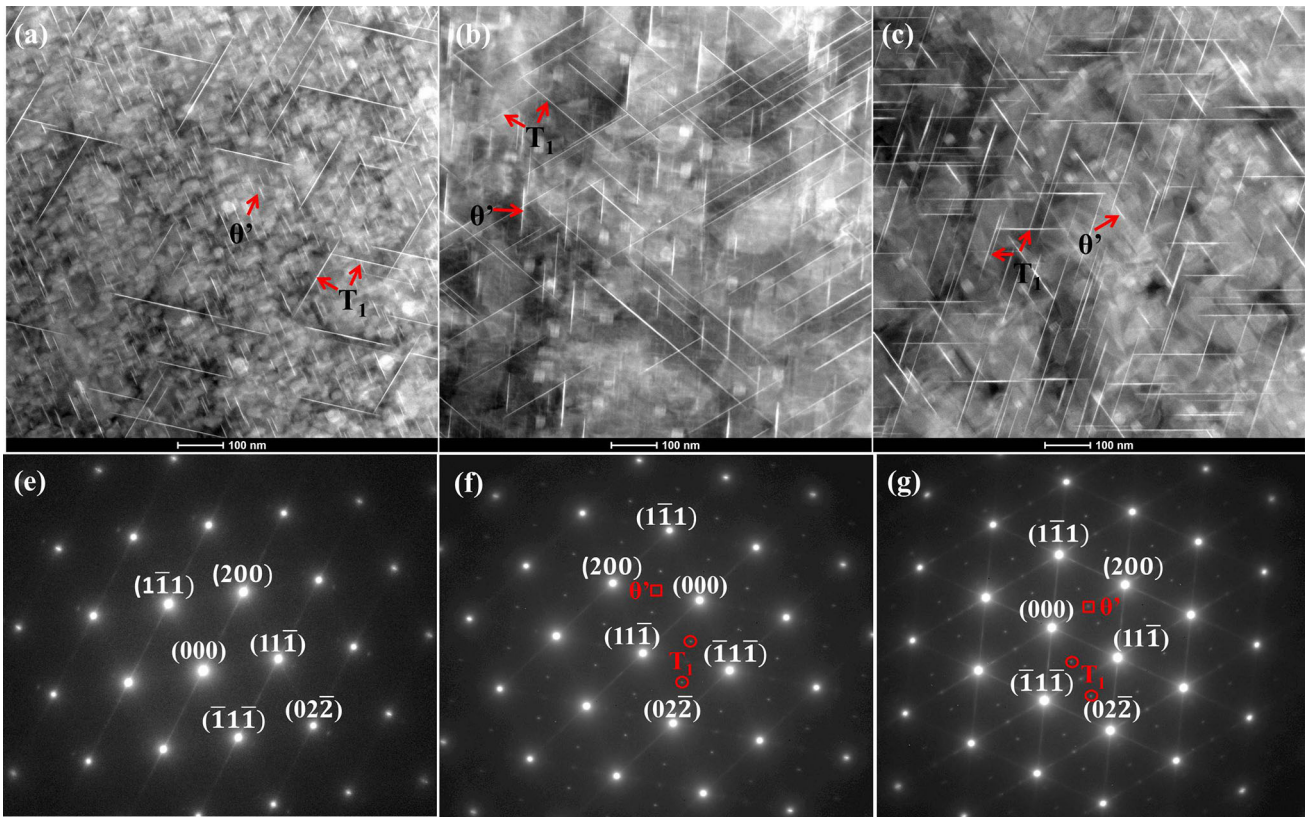
Fig. 11 STEM images and the corresponding SAED patterns along $[011]_{Al}$ direction of the (a), (e) LTA; (b), (f) MTA; (c), (g) HTA samples
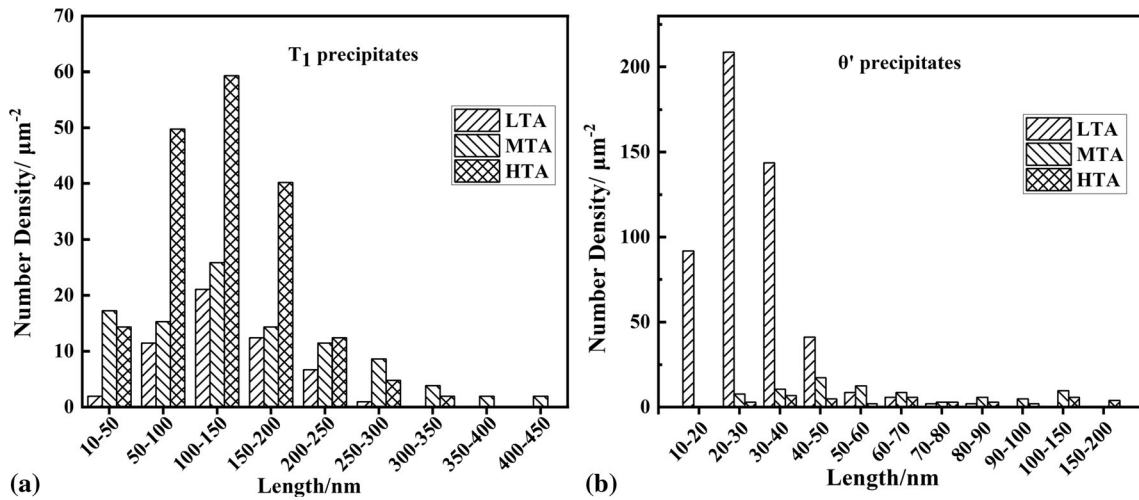

Fig. 12 (a) The length distribution of T_1 precipitates and (b) θ' precipitates within grains of different samples

Table 5 The statistical results of T_1 and θ' phases of peak-aged 2195 alloy

Aging condition	Number density/μm^{-2}		Average Width/nm		Average Length/nm		Area fraction/%	
	T_1	θ'	T_1	θ'	T_1	θ'	T_1	θ'
LTA	54.55	503.35	2.78	2.14	133.59	29.23	2.03	3.16
MTA	100.48	79.43	2.7	3.17	129.57	60.33	4.01	1.5
HTA	182.78	39.23	2.56	3.45	128.44	77.74	5.54	1.05
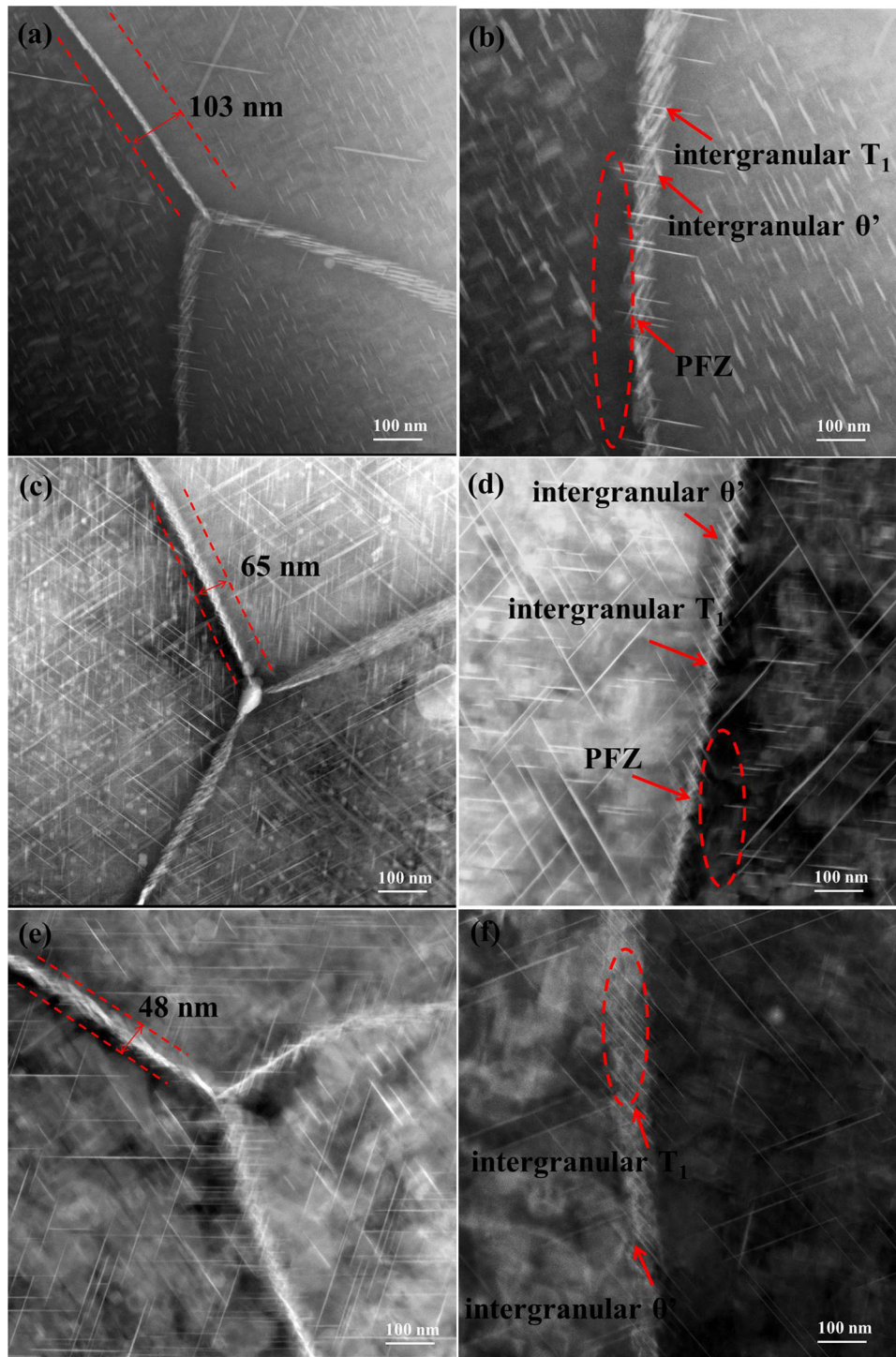
Fig. 13 Grain boundary precipitates and precipitate-free zone (PFZ) of the (a), (b) LTA; (c)(d) MTA; (e), (f) HTA samples

boundary precipitates in the HTA sample were further analyzed by EDX line-scanning, and the corresponding element distributions across the grain boundary region is shown in Fig. 14(b). Cu atoms were clearly segregated, indicating that the PFZ was depleted in Cu. The concentration of Cu along the grain boundary was higher due to T_1 and θ' phase precipitates. IGC resistance is associated with different concentrations of Cu atoms between grain boundary precipitates and adjacent zones (Ref 32). An active path was formed adjacent to the grain boundaries due to the depletion of Cu atoms, while a noble path formed along the Cu-enriched grain boundaries, which formed a continuous nanoscale microgalvanic path for IGC (Ref 33).
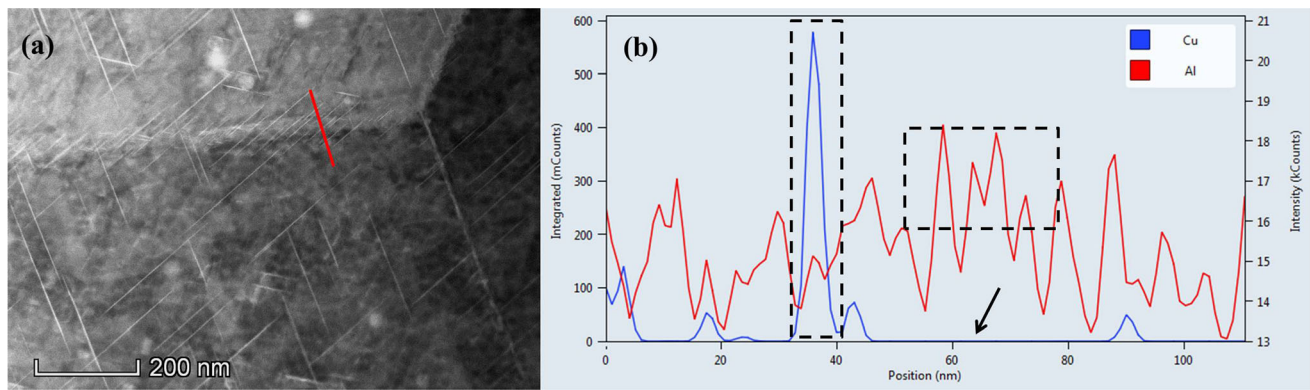
Fig. 14 (a) HAADF micrograph of a grain boundary in the HTA alloy; (b) EDS line of the grain boundary in (a)

4. Discussion

4.1 Influence of Aging Treatment on the Microhardness and Strength

As shown in Fig. 2 and 3, a higher aging temperature resulted in both a higher microhardness and tensile strength for the studied alloy. The mechanical properties of Al-Cu-Li alloys depend on the morphology and distribution of precipitates. The strengthening phases of the studied alloy are T_1 and θ', the distribution of which is responsible for the variation of mechanical properties (Fig. 11). The statistical results for the size and number density of precipitates show that the precipitation of the T_1 phase was accelerated by a higher aging temperature, while the θ' phase precipitation was inhibited because of the competitive relationship between these two phases (Fig. 12 and Table 5). Moreover, the competitive relationship between T_1 phases was also produced due to a lack of Cu atoms, which reduced the size of T_1 phases. It is known that the precipitation strengthening is highly dependent on interactions between precipitates and dislocations (Ref 5). The T_1 phase is bypassed by dislocations, which increases the strength due to fine homogeneous slip on the operating slip plane; however, the θ' phase is sheared by dislocations, resulting in coarse planar slip, which has a weaker strengthening effect compared with the T_1 phase. According to the model proposed by Huang and Ardell (Ref 34), both the shearing mechanism and bypassing mechanism can be described by the following equations:

$$\Delta\tau_{\mathrm{cut}} = \alpha f^{1/2} r^{1/2} \tag{Eq 1}$$

$$\Delta\tau_{\mathrm{bypass}} = \beta f^{1/2} r^{-1} \tag{Eq 2}$$

where $\Delta\tau$ is the critical shear stress, f and r are the number density and the radius of the precipitates, respectively, and α and β are constants.

In this work, the number density of the θ' phase decreased from 503.35 μm^{-2} to 79.43 and 39.23 μm^{-2}, but the dominant size increased upon increasing the aging temperature, resulting in a weaker work hardening effect. The combined effects of both an increased number density and the decreased dominant size of the T_1 phase improved both the strength and hardness of the studied alloy; therefore, the T_1 phase had a greater effect on the mechanical properties than the θ' phase, which indicated that the dominant strengthening phase was T_1 precipitates. Similar results were obtained by Wang (Ref 35), who ascribed the acceleration of the aging strengthening response to more rapid T_1 phase precipitation.

4.2 Influence of Aging Treatment on the Corrosion Susceptibility

The corrosion test results showed that the HTA sample was much more susceptible to corrosion than other samples (Fig. 5 and 7). According to previous studies on the corrosion susceptibility of Al-Cu-Li alloys, the distribution and number density of T_1 phases are responsible for IGC (Ref 4, 5, 16, 31). On one hand, the T_1 phase formed along the grain boundary consumed many Cu atoms, resulting in Cu depletion in the PFZ. Then, the PFZ acted as the cathode with respect to the Cu-enriched area. An increase in the number density of T_1 phases by continuing aging increased the electrochemical driving force between the intermetallic particles, which favored IGC corrosion (Ref 36). As the T_1 phases at the grain boundary dissolved, the presence of an intragranular T_1 phase acted as the anode with respect to the grain boundary, which caused intragranular corrosion (Ref 15). On other hand, it was demonstrated that the corrosion potential of the aluminum matrix (-0.75 V_{SCE}) was much more positive than that of the T_1 phase (-1.076 V_{SCE}) (Ref 37). Therefore, the presence of continuously-distributed T_1 phases along the grain boundary decreased the corrosion potential of the grain boundary to more negative values. Galvanic coupling occurred due to potential differences (PD) between grain boundary precipitates and the adjacent area, which caused the grain boundary to be preferentially attacked, which improved the IGC susceptibility (Ref 38).

On the basis of above analysis, it is concluded that two types of corrosion occur: (i) the PFZs and grain boundary precipitates (GBPs) and (ii) the matrix and the GBPs. When the GBPs dissolves, the intergranular corrosion turns to intragranular corrosion. The IGC susceptibility is relevant to the number density of intergranular T_1. A higher aging temperature promoted the precipitation of T_1 phase both along the grain boundary and in the grain interior (Fig. 11 and 13). As a result, T_1 phase formed rapidly along the grain boundary as the aging temperature increased, resulting in a greater Cu depletion in the PFZ and a greater PD between grain boundary precipitates and the matrix, which accounted for the higher IGC susceptibility of the HTA samples.

According to Fig. 13, a lower aging temperature produced wider PFZs (103 nm for the LTA sample, 65 nm and 48 nm for the MTA and HTA sample, respectively), as well as discontinuously-distributed T_1 phase along the grain boundary. Importantly, the corrosion resistance was improved by the wider PFZs (Ref 10), and the increased number of discontinuous grain boundary precipitates (GBPs) also improved the IGC resistance (Ref 28). This is why the LTA sample displayed better IGC resistance than MTA and HTA samples. Similar results have been demonstrated in other alloys, such as 2099, 7085, and the 304H steel (Ref 17, 39, 40).

In addition, it was interesting that the different concentrations of Cu atoms in the grain boundaries and grain interior could be accounted for the different corrosion susceptibility of the studied alloy (Fig. 5 and 8). Zhang et al. (Ref 27) proposed that chemical heterogeneity affects the intergranular corrosion susceptibility of AA 2024. Ma et al. (Ref 41) found that localized corrosion propagation was correlated with the state of alloying elements during potentiodynamic polarization. Such results were in accordance with another study (Ref 15), in which the authors explained that the strong anodic susceptibility of 2050 alloy was associated with the redistribution of alloying elements. Thus, the IGC susceptibility is associated with chemical heterogeneity. Further investigation on how this chemical heterogeneity affected the IGC, and electrochemical corrosion is needed.

4.3 Correlation of the IGC Sensitivity with OCP

Combining the IGC images (Fig. 5) and OCP (Table 4), it was interesting that the higher IGC sensitivity was related to the more negative OCP. Such phenomenon lies in the fact that the OCP values are directly controlled by the volume fraction of T_1 precipitates—the more T_1 precipitates there are, the more negative the OCP is (Ref 42). The OCP value decreased upon increasing the aging temperature in this work, which was attributed to an increase in the number density of T_1 precipitates. Therefore, the LTA sample has the largest OCP of about −0.53 V, whereas those of MTA and HTA samples were about −0.64 V and −0.65 V, respectively. Moreover, according to the model proposed by Huang et al. (Ref 43) relating OCP evolution to observed corrosion mode, different OCPs lead to different types of corrosion. It was suggested that pitting corrosion occurred when the OCP varied from −0.59 V to −0.64 V. The corrosion type changed from pitting to general IGC at more negative OCPs (−0.64 V to −0.68 V). As shown in Fig 5 and 6, our results appear to be consistent with this model, because the corrosion of the studied alloy undergoes the change of pitting to IGC upon decreasing the OCP value.

5. Conclusions

(1) Precipitation strengthening in the peak-aged 2195 Al-Cu-Li alloy depended on the two main precipitates, T_1 and θ' phase, which displayed a competitive precipitation relationship. Upon increasing the aging temperature, the number density of the T_1 phase increased, and the size slightly decreased. For the θ' phase, the opposite trend was obtained.

(2) The microhardness and strength of the studied alloy significantly increased at higher aging temperatures, while the ductility decreased. The MTA sample displayed a good combination of microhardness and strength with little sacrifice in its ductility.

(3) An increase in the intergranular corrosion sensitivity, as well as a drop in the OCP of the studied alloy showed a correlation between them. Compared with the MTA and HTA samples, the LTA sample exhibited a higher IGC resistance. This was attributed to the presence of intergranular T_1, as well as the different concentrations of Cu atoms at the grain boundary and grain interior.

References

1. K. Yan, T.Y. Wang and H.M. Liang, Effects of Rotation Speed on Microstructure and Mechanical Properties of 2060 Al-Cu-Li Alloy in Friction Stir Welding, *J. Mater. Eng. Perform.*, 2018, **11**, p 5803–5814
2. K.R. Emil, D. Uyime and A. Victor, The Effect of Acid Pickling on the Corrosion Behavior of a Cerium Conversion-Coated AA2198-T851 Al-Cu-Li Alloy, *J. Mater. Eng. Perform.*, 2020, **1**, p 167–174
3. H. Ning, J.F. Li and P.C. Ma, Evolution of Aging Precipitates in an Al-Cu-Li Alloy with 1.5 wt% Li Concentration, *Vacuum.*, 2020, **182**, p 109677
4. Y.X. Wang, X.W. Ma and H.K. Xi, Effects of Pre-stretching and Aging Treatments on Microstructure, Mechanical Properties, and Corrosion Behavior of Spray-Formed Al-Cu-Li Alloy 2195, *J. Mater. Eng. Perform.*, 2020, **10**, p 6960–6973
5. H.Y. Li, W. Kang and X.C. Lu, Effect of Age-forming on Microstructure, Mechanical and Corrosion Properties of a novel Al–Li alloy, *J. Alloys. Compd.*, 2015, **640**, p 210–218
6. J.S. Tao, L. Zhang and G.H. Wu, Effect of Heat Treatment on the Microstructure and Mechanical Properties of Extruded Al-4Cu-1Li-0.4Mg-0.4Ag-0.18Zr Alloy, *Mater. Sci. Eng. A.*, 2018, **717**, p 11–19
7. X.X. Chen, X.W. Ma and H.K. Xi, Effects of Heat Treatment on the Microstructure and Mechanical Properties of Extruded 2196 Al-Cu-Li Alloy, *Mater. Des.*, 2020, **192**, p 108746
8. V.A. Peters, B. Gault and F.D. Geuser, Microstructural Evolution during Ageing of Al-Cu-Li-x Alloys, *Acta Mater.*, 2014, **66**, p 199–208
9. J.F. Li, Z.H. Ye and D.Y. Liu, Influence of Pre-deformation on Aging Precipitation Behavior of Three Al–Cu–Li Alloys, *Acta. Metall. Sin. (Engl. Lett.)*, 2017, **30**, p 133–145
10. A. Medjahed, A. Henniche and M. Derradji, Effects of Cu/Mg Ratio on the Microstructure, Mechanical and Corrosion Properties of Al-Cu-Li-Cu-Mg-X Alloys, *Mater. Sci. Eng. A.*, 2018, **718**, p 241–249
11. A.T. Chen, G.H. Wu and L. Zhang, Microstructural Characteristics and Mechanical Properties of Cast Al-3Li-xCu-0.2Zr Alloy, *Mater. Sci. Eng. A.*, 2016, **677**, p 29–40
12. B. Chen, C.H. Li and S.C. He, Corrosion Behavior of 2099 Al-Cu-Li Alloy in NaCl Aqueous Solution, *J. Mater. Res.*, 2014, **12**, p 1344–1353
13. C.S. Lee and P.I. Choi, Stress Corrosion Cracking Behavior of Al-Cu-Li-Mg-Zr(-Ag) Alloys, *Met. Mater. Int.*, 2002, **8**, p 191–196

14. M. Guérin, E. Andrieu and G. Odemer, Effect of Varying Conditions of Exposure to an Aggressive Medium on the Corrosion Behavior of the 2050 Al-Cu-Li Alloy, *Corrosion Sci.*, 2014, **85**, p 455–470

15. V. Proton, J. Alexis and E. Andrieu, The Influence of Artificial Ageing on the Corrosion Behaviour of a 2050 Aluminium-Copper-Lithium Alloy, *Corrosion Sci.*, 2014, **80**, p 494–502

16. Y. Lin, C. Lu and C.Y. Wei, Effect of Aging Treatment on Microstructures, Tensile properties and Intergranular Corrosion Behavior of Al-Cu-Li Alloy, *Mater. Charact.*, 2018, **141**, p 163–168

17. Y. Ma, X. Zhou and Y. Liao, Localised Corrosion in AA 2099–T83 Aluminium-Lithium Alloy: The Role of Grain Orientation, *Corrosion Sci.*, 2016, **107**, p 41–48

18. X.X. Zhang, X.R. Zhou and T. Hashimoto, Corrosion Behaviour of 2A97-T6 Al-Cu-Li alloy: The Influence of Non-uniform Precipitation, *Corrosion Sci.*, 2018, **132**, p 1–8

19. U. Donatus, M. Terada and C.R. Ospina, On the AA2198-T851 Alloy Microstructure and its Correlation with Localized Corrosion Behavior, *Corrosion Sci.*, 2018, **131**, p 300–309

20. P.S. Chen and B.N. Bhat, Time-Temperature-Precipitation Behavior in Al-Li Alloy 2195, NASA technical report, 211548, 2002

21. H.Y. Li, D.S. Huang and W. Kang, Effect of Different Aging Processes on the Microstructure and Mechanical Properties of a Novel Al-Cu-Li Alloy, *J. Mater. Sci. Technol.*, 2016, **32**, p 1049–1053

22. H.J. Kim and M. Niinomi, The Role of Microstructures on the Strengthening Mechanisms of a Thermomechanically Processed 2091 Al–Li alloy, *Mater. Sci. Eng. A.*, 2000, **284**, p 14–24

23. B. Jiang, F.H. Cao, H.S. Wang, D.Q. Yi and Y. Jiang, Effect of Aging Time on the Microstructure Evolution and Mechanical Property in an Al-Cu-Li Alloy Sheet, *Mater. Sci. Eng. A.*, 2019, **740–741**, p 157–164

24. B. Decreus, A. Deschamps and F. Geuser, Influence of Natural Ageing and Deformation on Precipitation in an Al-Cu-Li Alloy, *Adv. Eng. Mater.*, 2013, **11**, p 1082–1085

25. S.F. Zhang, W.D. Zeng and W.H. Yang, Ageing Response of a Al–Cu–Li 2198 Alloy, *Mater. Des.*, 2014, **63**, p 368–374

26. J.F. Li, J.L. Huang and D.Y. Liu, Distribution and Evolution of Aging Precipitates in Al-Cu-Li Alloy with High Li Concentration, *Trans. Nonferrous Met. Soc. China.*, 2019, **29**, p 15–24

27. X.X. Zhang, Y.B. Jiao and Y. Yu, Intergranular Corrosion in AA2024-T3 Aluminium Alloy: The Influence of Stored Energy and Prediction, *Corrosion Sci.*, 2019, **155**, p 1–12

28. G. Svenningsen, J. ErikLein and A. Bjørgum, Effect of Low Copper Content and Heat Treatment on Intergranular Corrosion of Model AlMgSi Alloys, *Corrosion Sci.*, 2006, **48**, p 226–242

29. X.H. Xu, Y.L. Deng and S.Q. Chi, Effect of Interrupted Ageing Treatment on the Mechanical Properties and Intergranular Corrosion Behavior of Al-Mg-Si Alloys, *J. Mater. Res. Technol.*, 2020, **9**, p 230–241

30. J. Zhang, C. Wang and Y. Zhang, Effects of Creep Aging upon Al-Cu-Li Alloy: Strength, Toughness and Microstructure, *J. Alloy. Compd.*, 2018, **764**, p 452–459

31. B. Jiang, H.S. Wang and Y. Tian, Effects of Aging Time on Corrosion Behavior of an Al-Cu-Li Alloy, *Corro Sci.*, 2020, **173**, p 108759

32. S.L. Hou, D. Zhang and Y.L. Pan, Dependence of Microstructure, Mechanical Properties, and Intergranular Corrosion Behavior of Al-5.1Mg-3.0Zn-0.15Cu Alloys with High Temperature Pre-treatment, *Mater. Charact.*, 2020, **168**, p 110512

33. G. Svenningsen, M.H. Larsen, J.H. Nordlien and K. Nisancioglu, Effect of Thermomechanical History on Intergranular Corrosion of Extruded AlMgSi(Cu) Model Alloy, *Corros. Sci.*, 2006, **48**, p 3969–3987

34. J.C. Huang and A.J. Ardell, Precipitation Strengthening of Binary Al–Li Alloys by δ' Precipitates, *Mater. Sci. Eng. A.*, 1988, **104**, p 149–156

35. X.H. Wang, J.H. Wang, Xin Yue and Y. Gao, Effect of Aging Treatment on the Exfoliation Corrosion and Stress Corrosion Cracking Behaviors of 2195 Al-Cu-Li Alloy, *Mater. Des.*, 2015, **67**, p 596–605

36. G. Svenningsen, M.H. Larsen and J.C. Walmsley, Effect of Artificial Aging on Intergranular Corrosion of Extruded AlMgSi Alloy with Small Cu Content, *Corrosion Sci.*, 2006, **48**, p 1528–1543

37. J.F. Li, C.X. Li and Z.W. Peng, Corrosion Mechanism Associated with T_1 and T_2 Precipitates of Al-Cu-Li Alloys in NaCl Solution, *J. Alloy. Compd.*, 2008, **460**, p 688–693

38. M. Guérin, J. Alexis and E. Andrieu, Identification of the Metallurgical Parameters Explaining the Corrosion Susceptibility in a 2050 Aluminium Alloy, *Corrosion Sci.*, 2016, **102**, p 291–300

39. Y. Zou, L.F. Cao and X.D. Wu, Effect of Ageing Temperature on Microstructure, Mechanical Property and Corrosion Behavior of Aluminum Alloy 7085, *J. Alloy. Compd.*, 2020, **823**, p 153792

40. L.M. Yao and R.K. Wang, Influences of Nano-structured Thermal Stability on the Intergranular Corrosion of High-Carbon Austenitic Heat-Resistant Steel, *J. Mater. Eng. Perform.*, 2021, **1**, p 783–793

41. Y.L. Ma, X.R. Zhou and X.M. Meng, Influence of Thermomechanical Treatments on Localized Corrosion Susceptibility and Propagation Mechanism of AA2099 Al-Cu-Li Alloy, *Trans. Nonferrous Met. Soc. China.*, 2016, **26**, p 1472–1481

42. Z.X. Wang, P. Chen and H. Li, The Intergranular Corrosion Susceptibility of 2024 Al Alloy during Re–ageing after Solution Treating and Cold–rolling, *Corrosion Sci.*, 2017, **114**, p 156–168

43. J.L. Huang, J.F. Li, D.Y. Liu, R.F. Zhang, Y.L. Chen, X.H. Zhang, P.C. Ma, R.K. Gupta, and N. Birbilis, Correlation of Intergranular Corrosion Behaviour with Microstructure in Al-Cu-Li Alloy, *Corrosion Sci.*, 2018, **139**, p 215–226